Shear banding-activated dynamic recrystallization and phase transformation during quasi-static loading of β-metastable Ti – 12 wt % Mo alloy

Shear banding-activated dynamic recrystallization and phase transformation during quasi-static loading of β-metastable Ti – 12 wt % Mo alloy

L. Choisez[1,4], L. Ding[1,2,3,4], M. Marteleur[1], A. Kashiwar[1,2], H. Idrissi[1,2], P.J. Jacques[1]

1 UCLouvain, Institute of Mechanics, Materials and Civil Engineering, IMAP, Place Sainte Barbe, 2, B-1348 Louvain-la-Neuve, Belgium.

2 Department of Physics, Electron Microscopy for Materials Science (EMAT), University of Antwerp, Groenenborgerlaan 171, 2020 Antwerpen, Belgium.

3 Now at: Key laboratory for Light-weight Materials, Nanjing Tech University, Nanjing 211816, China

4 The authors contributed equally to the work

Abstract

Dynamic recrystallization (DRX) within adiabatic shear bands forming during the fracture of TRIP-TWIP β−metastable Ti-12Mo (wt %) alloy was recently reported. The formation of 1-3 µm thick-adiabatic shear bands, and of dynamic recrystallization, was quite surprising as their occurrence generally requires high temperature and/or high strain rate loading while these samples were loaded in quasi-static conditions at room temperature. To better understand the fracture mechanism and associated microstructural evolution, thin foils representative of different stages of the fracture process were machined from the fracture surface by Focused Ion Beam (FIB) and analyzed by Transmission Electron Microscopy (TEM) and Automated Crystal Orientation mapping (ACOM-TEM). Complex microstructure transformations involving severe plastic deformed nano-structuration, crystalline rotation and local precipitation of the ω_{ath} phase were identified. The spatial and temporal evolution of the microstructure during the propagation of the crack was explained through dynamic recovery and continuous dynamic recrystallization, and linked to the modelled distribution of temperature and strain level where TEM samples were extracted.

1. Introduction

Specific β-metastable Ti alloys designed for presenting simultaneously transformation induced plasticity (TRIP), twinning-induced plasticity (TWIP) and dislocation glide during straining exhibit superior combinations of strength and ductility [1]–[8]. While the deformation mechanisms of this new family of TRIP-TWIP β-metastable Ti alloys has been intensively investigated [1]–[8], their fracture behavior received less attention. The fracture mechanism of the Ti-12wt % Mo alloy (noted Ti-12Mo in the following), the most representative alloy of this family, was thoroughly scrutinized recently [9]–[11], revealing that during quasi-static tensile loading, its fracture is dominated by strain localization in a thin adiabatic shear band, after localized necking. A very large temperature rise close to the melting temperature of the alloy was measured during fracture, and was related to the very large cracking speed [9], [10]. The reached temperature induces a local decrease of the viscosity of the alloy, inducing a transition from a solid-state to a viscous-state in the fracture zone, bringing an original fracture surface presenting Taylor meniscus patterns [11]. Taylor meniscus patterns are indeed normally only observed during fracture of metallic glasses, polymers and liquid interfaces, resulting from the penetration of a less viscous fluid (like air) during the separation of a fluid layer between two solid surfaces [12], [13]. Finally, dynamic recrystallization (DRX), observed post-mortem beneath the fracture surface [9], was related most probably to the large deformation level at fracture and to this temperature rise in the shear band.

Dynamic recrystallization is generally related to three different mechanisms [14], [15], i.e. discontinuous dynamic recrystallization (dDRX), continuous or rotational dynamic recrystallization (cDRX/rDRX), and geometrical dynamic recrystallization (gDRX). It is worth noting that discontinuous dynamic recrystallization (dDRX) is the only mechanism corresponding to the classical definition of recrystallization, with the nucleation of new grains on sites of largest densities of defects and their subsequent growth. The microstructure resulting from dDRX consists generally of wavy large deformed grains with necklaces of new recrystallized grains [14], [16]. Continuous dynamic recrystallization (cDRX/rDRX) corresponds to the continuous formation of new grains by rotation of elongated structures until a large misorientation is reached [14], [17], [18]. The rotation of the elongated structures occurs as the result of the accumulation of dislocations at the elongated structure boundaries. A large level of deformation is thus generally required. The resulting microstructures consist in homogeneous equiaxed grains, generally of the same size as the elongated structures previously formed [17], [18]. It was argued that continuous dynamic recrystallization would be better referred as an extended recovery process because of the important role of recovery in the formation of the elongated structures, and the lack of distinct recrystallization front [15]. Nevertheless, cDRX is classically considered as a dynamic recrystallization process in the literature [17], [18] as it results in the formation of new small grains free from dislocations, separated by high angle grain boundaries, especially when additional migration of boundaries is involved [15]. It is also worth noting that cDRX is mostly reported in studies related to severe plastic deformation techniques like accumulative roll bonding [10], torsion [19], hot rolling [20], ... Geometrical dynamic recrystallization (gDRX) consists in the formation of new grains from thin elongated grains, from the pinching of the inward serrations of two opposite grain boundaries, and has been mostly observed in Al alloys [21].

In the specific case of Ti alloys, the activated mechanism of dynamic recrystallization is still the topic of numerous studies. Nucleation and growth of new grains by dDRX is commonly considered when modeling the dynamic recrystallization of titanium alloys during hot working [16], [22]. However, DRX is generally interpreted as a cDRX/rDRX mechanism in α, $\alpha+\beta$ and β Ti alloys, both during hot working and dynamic loading [23]–[26]. Some authors also reported the activation of two different DRX mechanisms at the same time: both dDRX and cDRX were reported during the dynamic compression of a $\alpha+\beta$ Ti alloy [27] and during hot rolling of a near β Ti alloy [28]. Chen *et al.* [29] claimed that dDRX occurred during the hot compression of $\beta-$ annealed lamellar TC11 alloy, forming necklaces of recrystallized grains around the elongated original grains, together with gDRX inside the elongated grains with serrated grain boundaries. Montheillet *et al.* [19] on the other hand, interpreted the DRX occurring during the hot deformation of a β Ti alloy as both gDRX and cDRX. The type of dynamic recrystallization mechanism activated during adiabatic shear banding in Ti alloys is therefore not straightforward and requires further analysis.

Moreover, while most of the literature deals with dynamic recrystallization during dynamic loading in compression, torsion or forced shear, the dynamic recrystallization considered in the present study occurs at the end of a quasi-static tensile loading of the TRIP-TWIP β metastable Ti-12Mo alloy. The unstable fracture process involves adiabatic shear banding, offering locally the conditions for DRX, i.e. a large strain rate and increased temperature. Therefore, the initial strongly deformed microstructure and loading mode are very different from the conditions usually studied in the literature for DRX [19], [23]–[26], [28]–[30].

The present study thus deals with the modifications of microstructure occurring during fracture of Ti-12Mo, involving geometrical and temporal variations of temperature, deformation and deformation rate. TEM thin foils were extracted by FIB from the fracture surface to link the microstructure evolution during the crack propagation with its associate thermomechanical history. The occurrence of dynamic

recrystallization and phase transformations during shear banding were characterized by (high-resolution) TEM, as well as automated crystal orientation mapping in TEM (ACOM-TEM).

2. Experimental procedure

The Ti-12 wt % Mo alloy was cast into a slab ingot from commercially pure titanium and molybdenum by the self-consumable melting technique. The chemical composition after casting was measured as Ti-11.8 Mo-0.02 Fe-0.01 Cu-0.0115 O (in wt %) by Inductively Coupled Plasma (ICP-OES). The ingot was homogenized at 900°C for 15 minutes, followed by water quenching. It was then cold rolled down to 1.1 mm, corresponding to a thickness reduction level of 89%. An annealing treatment was carried out at 900°C for 15 minutes in high-purity Ar atmosphere, followed by water quenching. Figure 1 presents the initial microstructure, consisting of equiaxed β grains 41 ± 10 µm (Fig. 1(a)), and of nanoprecipitates of athermal ω phase (Fig. 1(b)).

Uniaxial tension was carried out on specimens with calibrated gauge length of 26 mm and gauge section of 1.1 × 6 mm² at a displacement rate of 1 mm.min^{-1}.

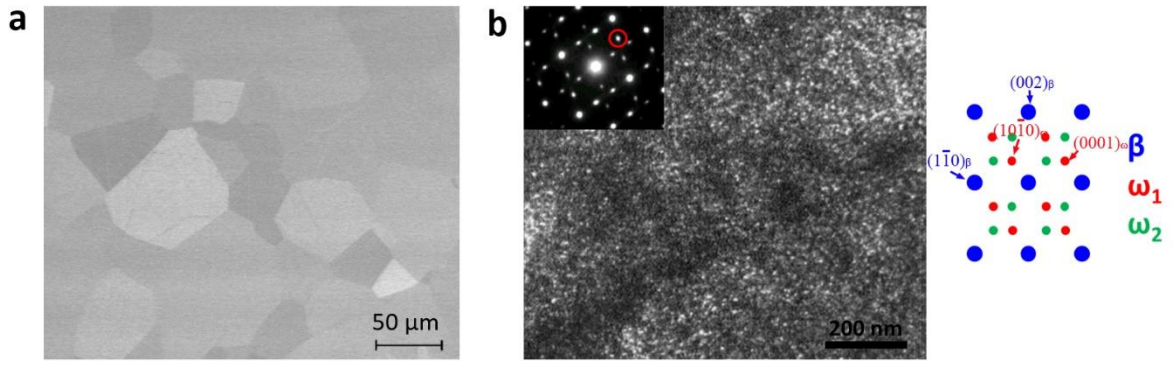

Figure 1: (a) Scanning electron micrograph of the initial microstructure, consisting of 40 µm β grains. (b) TEM micrograph of the initial microstructure with the associated diffraction pattern, showing the presence of nanoprecipitates of athermal ω (ω_{ath}) within the β phase. Inset gives the SAED pattern in the [110]$_\beta$ zone axis and the selected ω spot for observation of the ω precipitates.

Four TEM specimens were machined out of different regions of the fracture surface using a dual-beam focused ion beam (FIB) instrument (FEI Helios Nanolab 650). Figure 2 presents the fracture surface from which the TEM foils, labelled samples S1, S2, S3 and S4 in the following, were extracted. The location of these samples on the fracture surface was chosen to analyze the evolution of the microstructure resulting from the propagation of the crack, which can be associated with specific fracture features.

The location of the TEM samples was determined based on the fracture mechanism detailed in our previous studies [9], [11]. Fracture initiates from the surface of the sample by mode III shear, i.e. with the shear direction (globally through the thickness of the sample) perpendicular to the crack propagation direction (through the width of the sample). The location of sample S1 corresponds to the crack initiation site, at the extremity of a shear surface presenting ripples, which were associated with the first step of the fracture process [11]. The location of samples S2 and S3 corresponds to the propagation of the crack, both in terms of increasing distance from the crack initiation site along the width of the sample and in terms of increasing shear offset along the thickness of the sample, i.e.

further away from the edge of the fracture surface. The comparative distance of samples S1, S2 and S3 from the edge of the fracture surface is presented in Figure 2(f), representing their relative locations if they had been sampled in the same zone of the fracture surface. These fracture patterns are presented in higher magnification in Supplementary Figure S2. Sample S2 was extracted from a fracture feature highlighted by white arrows in Figs. 2(c), (d) and (f), corresponding to the transition between a shear process at the solid state and at the viscous state, as explained in our previous work [11]. The local transformation from the solid state to a viscous state was related to a local temperature rise during the fracture process, close to the melting temperature of the alloy [10]. After this particular fracture feature, Taylor meniscus patterns are sometimes observed on the fracture surface of this alloy, originating from the penetration of air inside the viscous layer formed by the local increase of the temperature. Sample S3 was machined out of the ridge of a Taylor meniscus pattern. Eventually, the end of the fracture process corresponds to the nucleation and growth of voids inside an adiabatic shear band formed during the unstable propagation of the crack, as detailed in our previous studies [9], [11]. The last sample was therefore FIB-machined from the wall of a dimple in the center of the fracture surface, to analyze the microstructure corresponding to the end of the fracture process.

The shear direction x involved in the fracture process is deduced from the shear lines observed on the fracture surface for samples S1, S2 and S3, and is indicated by a black arrow in Fig. 2 (b-d) [11]. The relative orientation of the width of the TEM lamella w on the fracture surface can be expressed as $w = \cos\theta\ x - \sin\theta\ y$, with x the shear direction and y the direction perpendicular to the shear direction on the fracture surface, and the angle θ equal to 0°, 15°, 98° and 90° for the TEM lamella S1, S2, S3 and S4, respectively. In the case of sample S4 (Fig. 2(e)), no shear line was visible, so the shear direction is taken as the global shear direction during a mode III fracture, i.e. along the thickness of the sample. The direction y perpendicular to the shear direction but included in the shear plane, i.e. in the fracture plane, is also indicated in Fig. 2 (b-e) as both directions x and y will be used to express the crystalline orientation of the grains regarding the shearing process. The local orientations of the TEM samples with respect to the tensile specimen are given in Supplementary Figure S1 and Supplementary Table 1.

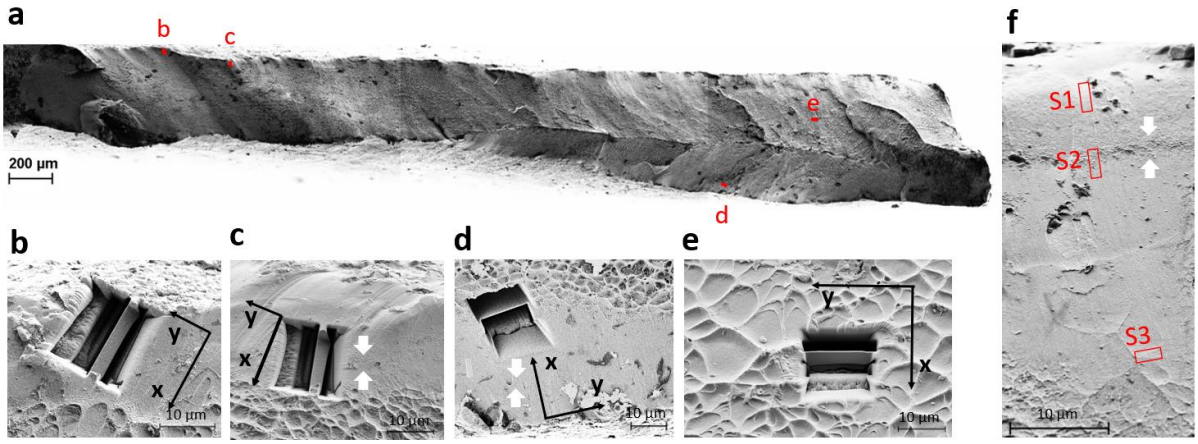

Figure 2: (a) Fracture surface of Ti-12Mo; (b-e) magnified views of the different locations where TEM foils were machined by FIB (S1, S2, S3 and S4 in (b), (c), (d) and (e), respectively). (f) Respective distance from the edge of the fracture surface (up) of samples S1, S2 and S3. The white arrows indicate the transition from a solid-state shear (up) and a viscous-like shear (down). The x and y directions correspond to the shear direction, and the direction perpendicular to the shear direction on the fracture surface.

The specimens were characterized by TEM using a FEI Tecnai G2 F20 transmission electron microscope operating at 200 kV. The ACOM-TEM technique was used in the same microscope equipped with the NanoMegas ASTAR system. For the ASTAR data acquisition, a probe size of 2.5nm, a precession angle of 0.4° and precession frequency of 100 Hz was used. The ACOM-TEM data were analyzed using the OIM TSL software from EDAX Inc. Low angle boundaries were considered for misorientation angles lower than 15° and high angle boundaries for misorientation angles larger than 15°. The orientation of the grains measured by ACOM-TEM was corrected to express the crystalline orientation of the cells with respect to the shear direction x. The inverse pole figures are expressed according to the shear direction x and to the direction y that is perpendicular to x and belonging to the shear plane.

3. Results

Figure 3 presents the uniaxial tensile true stress-true strain curve of Ti-12Mo. The true uniform strain is 0.3 while the true stress at maximum load is 930 MPa. The dotted line corresponds to the extrapolation of the stress-strain curve to the true fracture point. The true fracture strain and true fracture stress were estimated from the measurement of the reduction of area after fracture with respect to the initial section (see previous work for further details [11]).

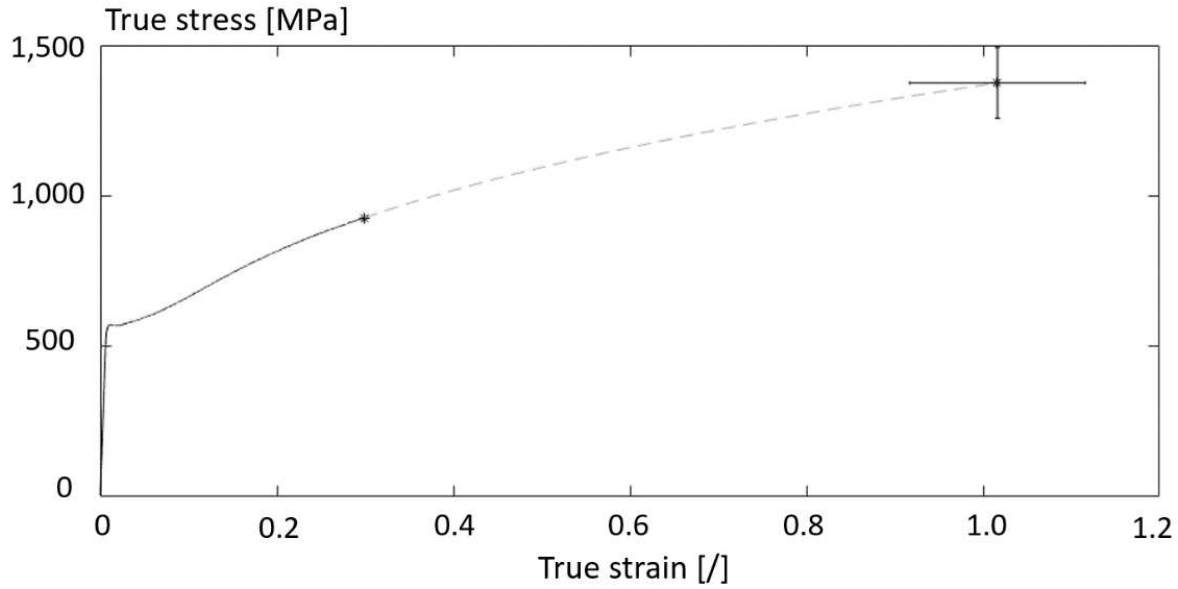

Figure 3: Uniaxial true stress – true strain curve of Ti-12Mo loaded at quasi-static strain rate.

Figure 4 presents the bright field micrographs and associated diffraction patterns of samples S1, S2, S3 and S4, respectively. Magnified micrographs of the zones with a finer microstructure, far from the fracture zone, are given in Figure S3 in the Supplementary Materials. Figure 4(a) shows the microstructure of sample S1 with a magnified view of the zone just below the fracture surface. A change in morphology characterized by a change of orientation of the constituting grains/cells close to the fracture surface can be observed (which will be confirmed by the ACOM-TEM maps of Figure 5). A dotted line has been drawn on Figure 4(a) to separate those two different zones noted S1-up (with a thickness increasing from 100nm to 250nm from right to left, i.e. when moving away from the fracture surface (Fig. 2b)) and S1-down in the following. Both zones present similar grain size distribution (Figure S4(a) in Supplementary Materials), with a mean grain size of 20 nm for zone S1-down and 24 nm for zone S1-up. However, the morphological orientation of the grains differs from zone S1-up to zone S1-down. The grains in zone S1-down are elongated in an oblique direction, at about 39° from the fracture surface, as highlighted by a white arrow in Fig. 4(a). On the other hand, the grains of zone S1-up are oriented parallel to the fracture surface, i.e. parallel to the shear direction. Finally, Figures 4(b) and 4(c) present the SAED diffraction patterns of zones S1-up and S1-down, respectively. Both diffraction patterns present a ring-like shape with a large angular spread of the diffraction spots. This pattern corresponds to a severely plastically deformed microstructure, where large gradients of crystal orientations are due to a large density of dislocations and to the presence of numerous interfaces. Brighter spots can however be observed on these SAED patterns, indicating the presence of cells with preferred crystallographic orientations. It is worth noting that the diffraction spots corresponding to the presence of ω_{ath} phase (highlighted in Fig. 1(b)) are not observed in both diffraction patterns of zones S1-up and S1-down (Figs. 4(b)-4(c)), indicating that ω_{ath} nanoprecipitates are not present in the microstructure of sample S1 anymore.

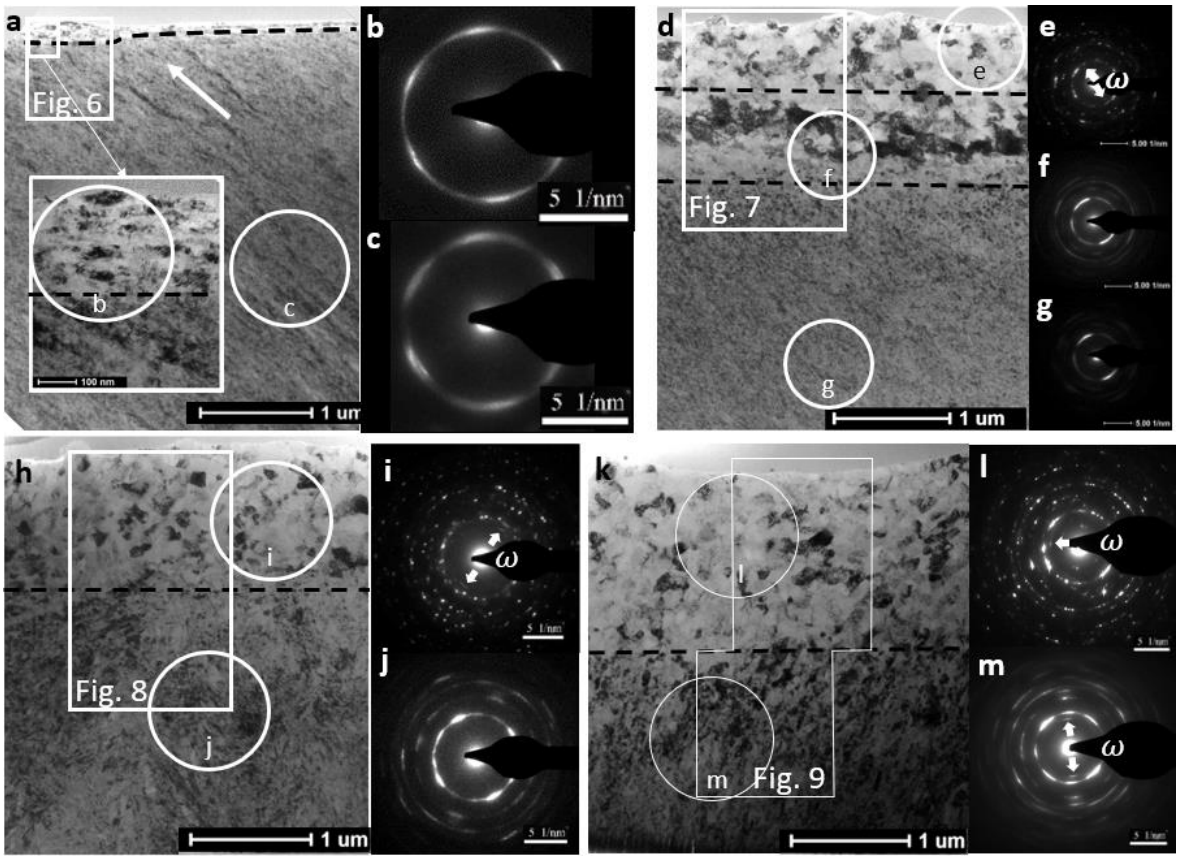

Figure 4: Bright-field TEM micrographs of (a) sample S1, (d) sample S2, (h) sample S3 and (k) sample S4, respectively. The dotted line separates zones of different microstructure, i.e. zones 'up' near the fracture surface and 'down' further away. A third zone, S2-middle, in-between zones S2-up and S2-down for sample S2. The diffraction patterns of each zone are given for (b-c) sample S1, (e-g) sample S2, (i-j) sample S3 and (l-m) sample S4

Figure 4(d) presents the bright field micrograph of sample S2. Three zones can be distinguished based on their morphologies and crystallography (as it will be highlighted in Figure 6 by the ACOM-TEM analysis). An upper 500 nm-thick zone called zone S2-up hereafter presents equiaxed grains, with the associated diffraction pattern (Fig. 4(e)) exhibiting well-defined diffraction spots. This diffraction pattern corresponds to the pattern of grains presenting well defined crystalline orientations. Furthermore, diffraction rings corresponding to the ω phase are clearly visible on this diffraction pattern. The associated spots are weak but the presence of ω_{ath} nanoprecipitates was confirmed by high-resolution TEM, as presented in Figure 5. The measured lattice parameters are a = 0.42 nm and c = 0.28 nm, which well correspond to the values reported in the literature [31].

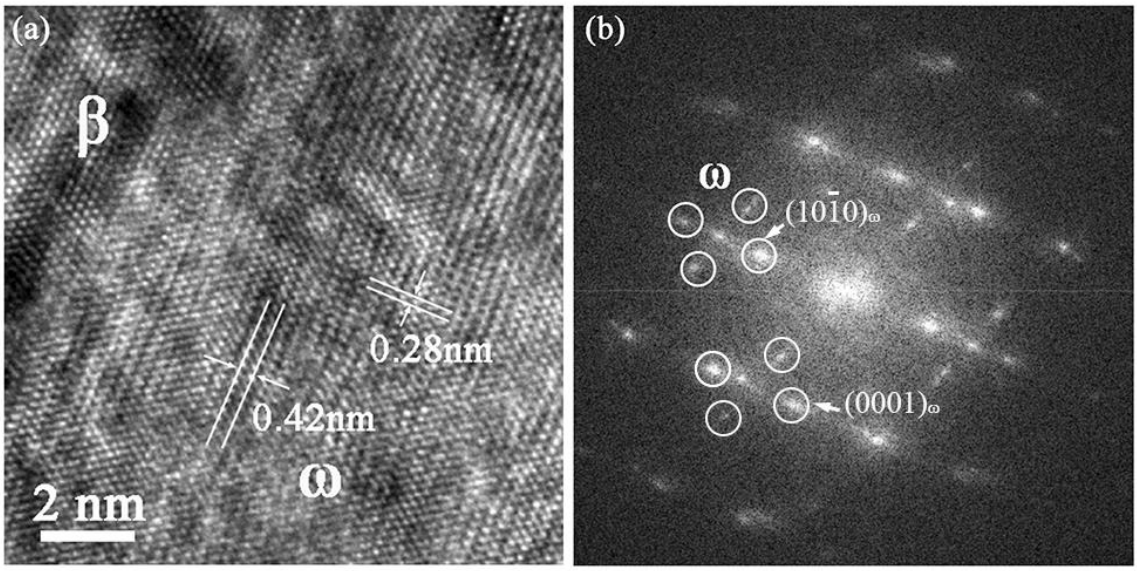

Figure 5: (a) HRTEM micrograph and (b) corresponding FFT pattern of the ω phase observed in zone S2-up (see Figure 4(d)).

A 850 nm-thick zone is present below zone S2-up, called zone S2-middle. This zone is composed of large elongated grains parallel to the shear direction (elongated grains with a width of 210 ± 70 nm), as better highlighted in the ACOM-TEM analysis in Figure 6. The zone underneath zone S2-middle, called S2-down hereafter, is composed of small grains with an average size of 16 nm, 3 times smaller than the average grain size of zone S2-up (48 nm). The grain size distributions are presented in Figure S4(b) in the Supplementary Materials. Figures 4(f) and 4(g) correspond to the diffraction patterns of these zones S2-middle and S2-down, presenting increasingly continuous rings with highly elongated diffraction spots. Contrarily to zone S2-up, the diffraction spots of ω_{ath} are no longer observed in these zones.

Figures 4(h) and 4(k) present the bright field micrographs of samples S3 and S4. A modified microstructure is observed near the fracture surface for both samples, with a thickness of 900 nm and 1600 nm for samples S3 and S4, respectively. These zones, called S3-up and S4-up hereafter, are both constituted of equiaxed grains with an average size of 59 nm and 56 nm, respectively. The zones underneath, called S3-down and S4-down, are constituted of smaller grains with an average grain size of 39 nm for both zones. Figures 4(i) and 4(l) present the diffraction patterns of zones S3-up and S4-up with well-defined diffraction spots similar to the ones of zone S2-up, i.e. well-defined spots of β grains as well as of the ω_{ath} phase. On the contrary, the diffraction patterns of zones S3-down and S4-down on Figures 4(j) and 4(m) exhibit spread of the diffraction spots of a deformed microstructure. Furthermore, no ω diffraction spots can be observed in the case of zone S3-down in Figure 4(j).

The output of the ACOM-TEM analysis of sample S1 corresponding to fracture initiation is given in Figure 6. Figures 6(a), 6(b) present the IPF maps while Figure 6(c) shows the grain boundary map. Zone S1-up and S1-down both present a similar microstructure consisting in elongated grains separated by high angle boundaries (HAGB) and containing several cells separated by low angle boundaries (LAGB). However, their morphological orientation differs as described in Figure 4(a), and both zones also differ by the dominant crystallographic orientation (Fig. 6(a)-(b)). Indeed, a shift from orientations close to <112> along the shear direction in zone S1-down to orientations close to <101> in zone S1-up is observed as highlighted in Fig. 6(d)-(e), while the crystalline direction <111> keeps pointing in the direction perpendicular to the shearing direction y. The transition from zone S1-down to zone S1-up thus corresponds to both a morphological rotation of the cell blocks and a rotation of the crystallographic orientation of the cells along the shear direction.

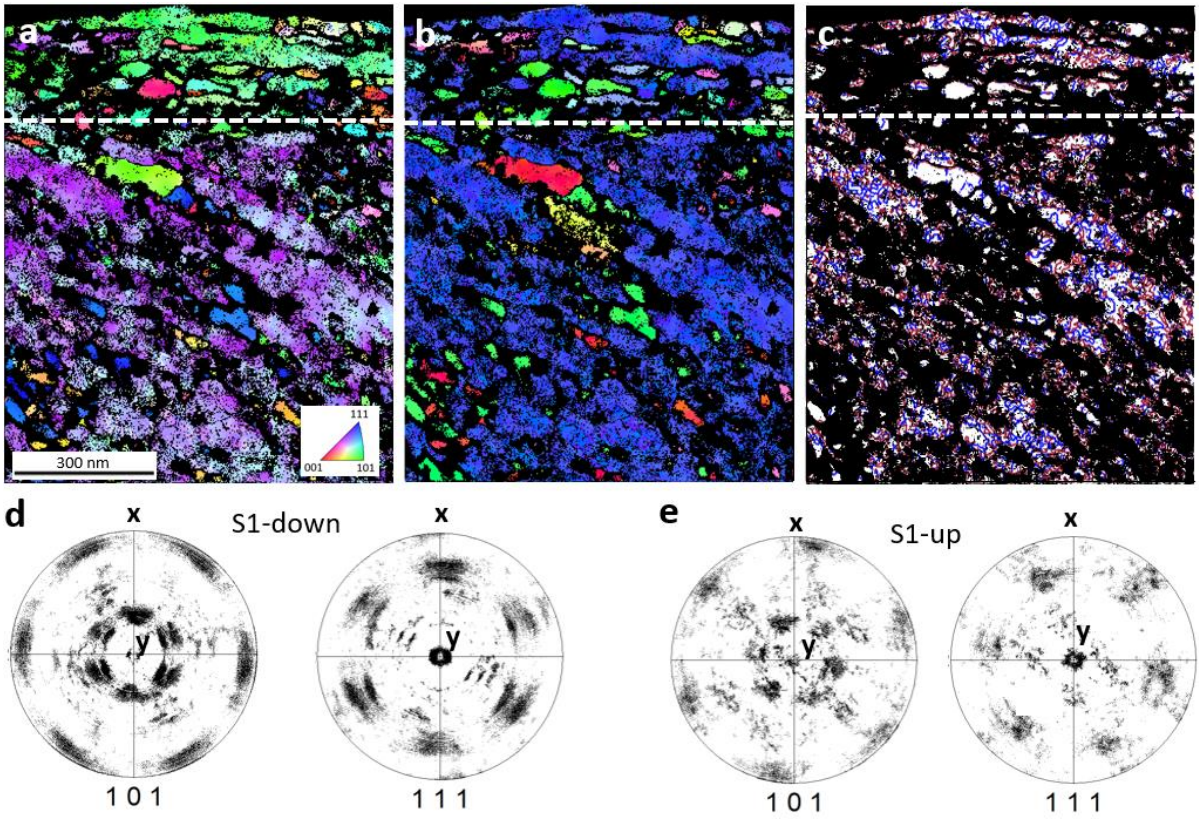

Figure 6: ACOM-TEM analysis of sample S1 (the analyzed zone is highlighted in Figure 4(a)). (a) Inverse pole figure maps corresponding to (a) the shear direction and (b) the direction perpendicular to the shear direction and parallel to the fracture surface. (c) Representation of high angle boundaries (red) and low angle boundaries (blue). (d) and (e) Pole figures of the zones S1-down and S1-up, respectively, with x and y directions defined in Figure 1.

The analysis of sample S2 corresponding to the propagation of the crack on the sheared surface associated with a larger temperature rise is given in Figure 7. Figures 7(a) and 7(b) correspond to the IPF maps, and Figure 7(c) shows the associated map highlighting low- and high-angle boundaries. While most grains are equiaxed in zone S2-up, some slightly elongated grains with concave shape can also be observed, separated by low angle boundaries in equiaxed cells as highlighted in the magnified view of Figure 7(d). A progressive increase of the misorientation of the grain boundaries is also observed by the transition from high angle boundary to low angle boundary along the same line, highlighted in the magnified view of Figures 7(d) and (e). Furthermore, orientations of the grains are rather random in zone S2-up. On the contrary, a preferred crystalline orientation is observed in zone S2-middle, with the small equiaxed grains at the transition between zones S2-down and S2-middle oriented in the same direction as the large elongated grains present in zone S2-middle. This crystalline orientation is similar to the one observed in zone S1-up, i.e. with orientations close to <101> parallel to the shear direction and orientations close to <111> perpendicular to the shear direction. It is also worth noting that this large elongated grain presents a progressive rotation of its crystal orientation along the shear direction as highlighted by Figure 7(f).

The ACOM-TEM analysis carried out on sample S3 is presented in Figure 8. Figures 8(a) and 8(b) correspond to the orientation maps of sample S3 while Figure 8(c) presents the associated grain

boundaries map. Zone S3-down is constituted of small equiaxed and elongated grains. Zone S3-up is similar to zone S2-up, predominantly composed of larger equiaxed grains, or elongated grains divided in equiaxed cells, with random orientations. An inset in Figure 8(c) highlights a concave grain separated into several equiaxed cells/grains by low angle and high angle boundaries. It is also worth noting that grains with random orientations are present in both zones.

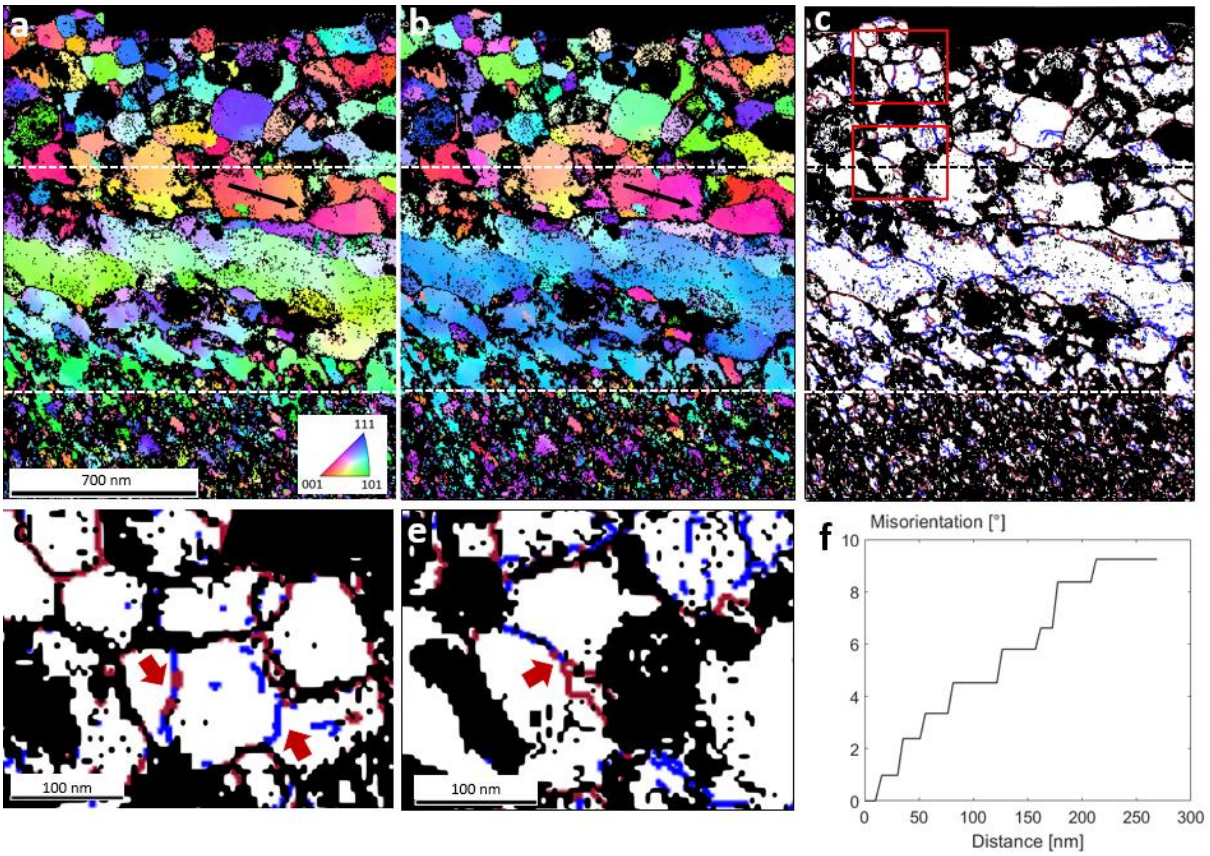

Figure 7: ACOM-TEM analysis of sample S2 (the zone highlighted in Figure 4(d)). (a) Inverse pole figure map corresponding to the shear direction and (b) the direction perpendicular to the shear direction and parallel to the fracture surface. (c) Representation of high angle boundaries (red) and low angle boundaries (blue), with (d-e) magnified views. (f) Misorientation gradient along the black arrow drawn in (a-b).

Finally, Figure 9 corresponds to sample S4, extracted from the middle of the fracture surface, i.e. with a dominant tensile fracture mode and a large temperature rise. The orientation maps (Figures 9(a) and 9(b)) and the grain boundary map (Figure 9(c)) reveal a similar microstructure as in the case of sample S3, with equiaxed grains of random orientation in zone S4-up. Zone S4-down is mostly composed of elongated grains divided in smaller cells. However, contrarily to zones S1-down, S2-down and S3-down, diffraction spots of ω_{ath} are visible for zone S4-down.

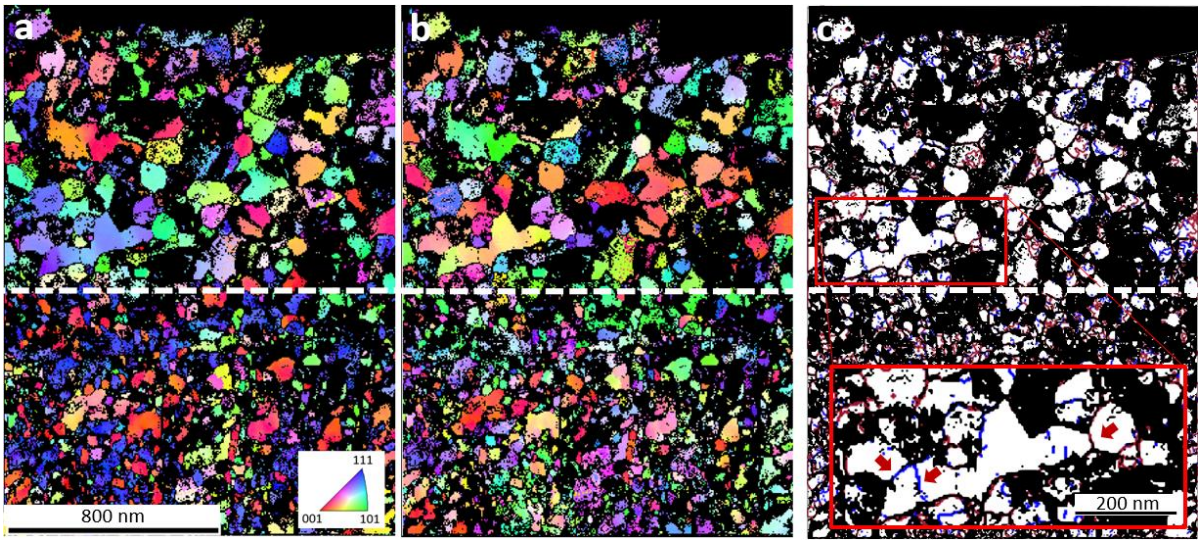

Figure 8: ACOM-TEM analysis of sample S3 (the zone highlighted in Figure 4(h)). (a) Inverse pole figure map corresponding to the shear direction and (b) the direction perpendicular to the shear direction and parallel to the fracture surface. (c) Distribution of high angle boundaries (red) and low angle boundaries (blue), with a magnified view of an elongated grain subdivided into equiaxed cells/grains.

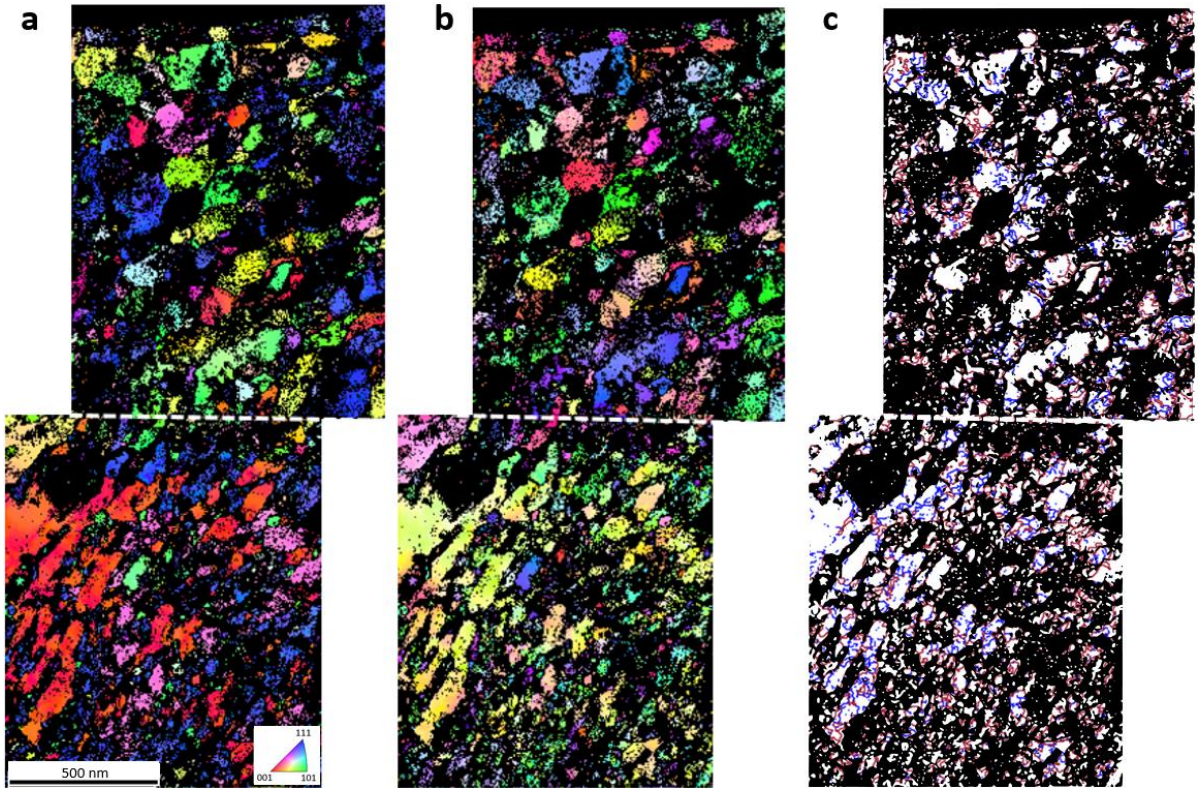

Figure 9: ACOM-TEM analysis of sample S4 (the zone highlighted in Figure 4(k)). (a) Inverse pole figure map corresponding to the shear direction and (b) the direction perpendicular to the shear direction and parallel to the fracture surface. (c) Distribution of high angle boundaries (red) and low angle boundaries (blue).

4. Discussion

4.1. Fracture-induced microstructure transformations

The TEM micrographs presented above clearly illustrate that the fracture process of Ti-12Mo brings important and complex modifications of the microstructure in the fracture zone. Figure 10 presents a schematic representation of the microstructures observed in the four TEM samples extracted underneath the fracture surface.

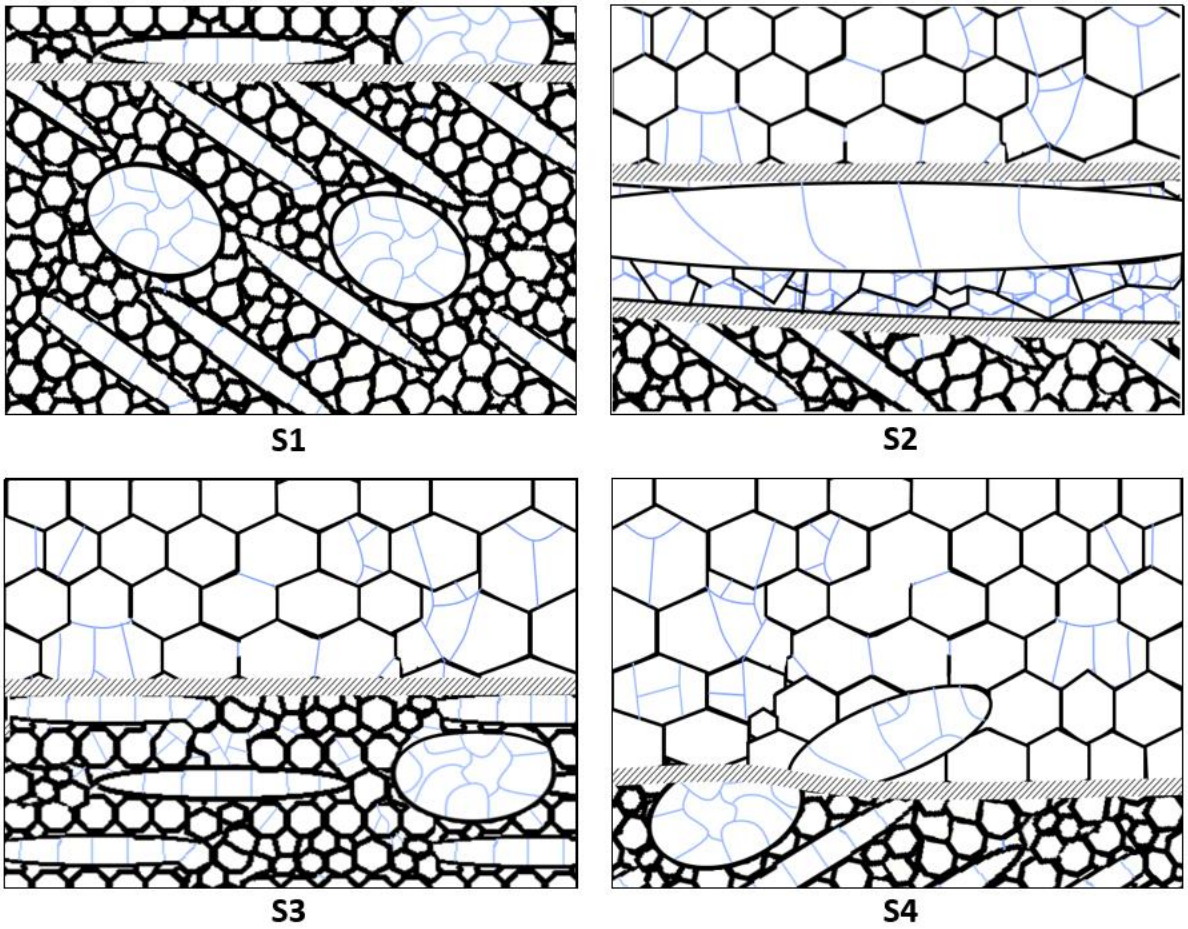

Figure 10: Schematic representation of the microstructure of the four TEM samples, with a dashed line separating the zones with different microstructures and with the HAGB and LAGB represented in black and blue, respectively.

Three zones can be distinguished presenting different microstructures. Firstly, a microstructure made of small equiaxed or elongated grains with a size smaller than 50 nm, containing several equiaxed cells and bringing about widespread diffraction rings typical of severely deformed microstructures (SPD), is found in sample S1, in zones S2-down, S3-down and S4-down. These zones (except zone S4-down (see below)) also share the common feature of the disappearance of the ω diffraction spots in the diffraction patterns, while ω_{ath} precipitates are initially present in the microstructure (Figure 1b). It

can be assumed that the ω_{ath} nanoprecipitates were completely dissolved by dislocation shearing, as it has been previously suggested for the decrease of the amount of ω_{ath} precipitates during the early stages of plasticity in Ti-12Mo [2] and scrutinized for ω_{iso} precipitates in localized deformation channels in several $\beta-$ Ti alloys [32], [33]. Secondly, the microstructure of zone S2-middle is constituted of large elongated grains parallel to the shear direction, which contain many LAGB, and small grains underneath with the same crystal orientation. This zone presents features typical of a recovered microstructure. Moreover, the central elongated grain is oriented with the <110> crystalline orientation and the {111} crystalline plane parallel to the shear direction, similar to the orientation of the grains in zone S1-up. This crystalline relationship between the grain orientation and the shear direction is typical of BCC materials after cold or hot rolling [34], and is often observed in β-Ti alloys at the beginning of hot rolling, before the activation of dynamic recrystallization [20], [35]. Furthermore, the large quantity of LAGB in zone S2-middle most probably results from the reorganization and annihilation of dislocations to decrease the internal energy of the system [36]. Therefore, it can be expected that this zone results from a dynamic recovery. Thirdly, zones S2-up, S3-up and S4-up present a similar microstructure, mostly constituted of larger equiaxed grains (with respect to zones S2-down, S3-down and S4-down). Their diffraction patterns present well-defined diffraction spots corresponding to a recrystallized microstructure with grains presenting distinguished crystal orientations. It is also worth noting that the width of this zone gradually increases from sample S2 to sample S4.

The type of dynamic recrystallization occurring during the adiabatic shear banding of Ti-12Mo shared more common features with the continuous dynamic recrystallization (cDRX) than with the classical nucleation and growth of new grains, i.e. discontinuous dynamic recrystallization (dDRX). Indeed, some of the grains present in the zones where recrystallization occurs present a concave shape and are separated by LAGB in which some cells have a convex equiaxed shape (Fig. 7(d)). Moreover, it was observed that some boundaries are partly LAGB and partly HAGB, indicating a progressive increase of the misorientation along these boundaries (Fig. 7(e), 8(c)). It can also be added that the formation of large elongated grains such as the ones observed in S2-middle was proposed by Nesterenko *et al.* [37] as a first step of continuous/rotational dynamic recrystallization during dynamic loading of tantalum, where the dislocations reorganized themselves to form large elongated cells, which then rotate to form HAGB. When these boundaries cannot accommodate additional dislocations, these ones are stored inside the grains, as observed in the large elongated grains of zone S2-middle (Fig. 7(c)) creating extra LAGB (Fig. 7(d)). According to the theory of cDRX, the crystal orientation of the different cells rotates up to the formation of new grains separated by HAGB and presenting different orientations. On the contrary, a discontinuous dynamic recrystallization by nucleation and growth of new grains would have produced an inhomogeneous microstructure with wavy deformed grains and sometimes necklaces of small new grains nucleated at their boundaries. The new grains would also present a convex equiaxed shape and would be completely separated by HAGB [17], [18].

Regarding crystal orientations, a strong texture generally results from discontinuous static recrystallization and discontinuous dynamic recrystallization in Ti alloys because of recrystallization sites of preferred orientations and/or favorable growth of preferred grain orientations [35], [38], [39]. On the other hand, a low texture intensity is regularly observed after continuous dynamic recrystallization as the new grains are formed with new orientations corresponding to a combination of rotation towards various activated glide dislocations systems [18], [20], [28], [40]. In this case, the relatively random orientations observed in the recrystallized zones support the hypothesis of cDRX.

Finally, cDRX is generally activated during dynamic loading at room temperature, when the strains localize in adiabatic shear banding. The estimated time at which a large temperature is reached is indeed very short (an estimation in the case of the fracture process of Ti-12Mo is given in the next

section in Table). It is physically impossible for dDRX to be at the origin of the recrystallized grains observed as the shearing time is too small to allow the growth of new nucleated grains [23], [24], [37], [41], [42]. dDRX is governed by thermally-activated mechanisms such as grain boundaries migration, while cDRX is governed by the level of deformation bringing accumulation of dislocations, although thermal activation is still necessary for the first step of cDRX in this case, i.e. dynamic recovery. Therefore, the occurrence of cDRX during fracture of Ti-12Mo would be favored by the strong shear localization, where the local shear deformation rate is very large and the time at high temperature short.

4.2. Thermomechanical history

The size, shape, orientation and defect contents of the grains are strongly varying over a very narrow distance for the different samples, as the result of the combined effects of plastic deformation and heat release accompanying the crack initiation and propagation. In order to fully explain these modifications of the microstructure occurring in samples S1 to S4, it is thus necessary to estimate as accurately as possible the fields of deformation and temperature accompanying the fracture process. The local strains and temperatures were estimated by using the tools developed in our previous work on the fracture of this alloy [10], [11] to the location of these TEM samples.

4.2.1. Strain evolution

Considering the whole deformation process, four deformation steps can be distinguished in the present Ti-12Mo alloy as developed in our previous work [11]: a first uniform deformation, followed by diffuse necking, localized necking, and finally shear banding in an adiabatic shear band, as schematically represented in Figure 11. At each step, the macroscopic deformation localizes in an always thinner region. Eventually, the material fractures within a 1-3 µm thick shear band. Zones S1-down, S2-down, S3-down and S4-down are thus located outside of the shear band, but still close to the fracture surface, at a distance ranging from 0.1-1 µm to 3 µm. They thus exhibit the microstructure resulting from localized necking, i.e. outside of the shear band. The local strain level there can be approximated by the true tensile fracture strain, i.e. $\epsilon \sim 1$. Obviously, this strain level only gives an averaged value for the whole fracture process. Indeed, a larger strain level is expected in the middle of the localized necking zone (sample S4) compared to the edge of the localized necking zone (sample S1) [43].

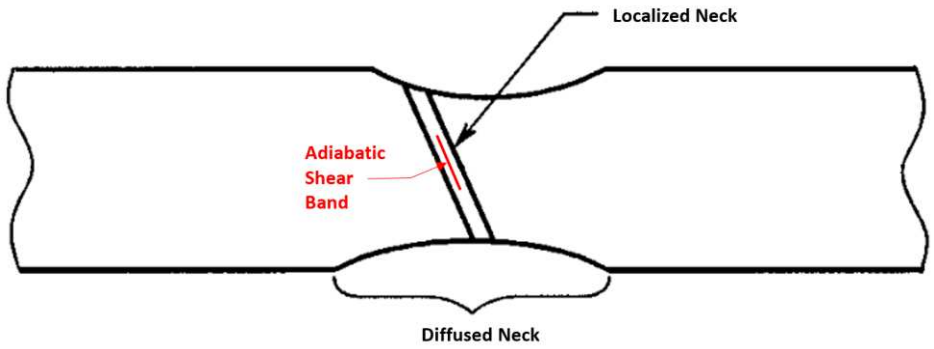

Figure 11: Schematic representation of the different steps of strain localization during uniaxial tensile deformation of Ti-12Mo.

The SPD microstructure observed in zones S1-up, S1-down, S2-down, S3-down and S4-down generally requires very high levels of deformation ($\epsilon_{min} \sim 6 - 7$) [44], [45]. However, the creation of a high density of interfaces can accelerate the process of microstructure refinement attributed to severe

plastic deformation. Zafari *et al.* [46] obtained a nanostructure in TRIP Ti-5553 alloy after a true strain of only 3. In the case of the present Ti-12Mo, the simultaneous activations of hierarchical TRIP and TWIP effects induces the formation of a very large density of interfaces with high angle misorientations already at small levels of strain [1], [2], [47]. Cells of about 50-100 nm in size are already present at the end of the uniform deformation, for $\epsilon \sim 0.3$ [9]. The size of these cells is further reduced after localized necking to a mean size of ~1-50nm (Figures 4, 6, 7, 8 and 9). The density of the network of interfaces strongly increasing with the level of deformation, and a typical SPD nanostructure is reached at a true strain of only 1 in the localized neck of Ti-12Mo.

The next step to consider is shear banding, and more particularly adiabatic shear banding for which both deformation and temperature have to be considered. The shear strain level is given by the ratio of the shear offset, i.e. the advance of the crack along the shear direction, and the thickness of the shear band. The shear offset for each TEM sample was measured on the fracture surface, corresponding to the distance between the TEM foil and the edge of the fracture surface. For sample S1, the half-thickness of the shear band is taken as the thickness of zone S1-up where the direction of elongation of the grains is parallel to the shear direction. In the case of samples S2, S3 and S4, the thickness of the band can no longer be estimated from the thickness of the zones S2-up, S3-up and S4-up because the recrystallization could occur on a larger depth than the actual shear band width. The thickness of the shear band is thus considered to be 1 ± 0.2 µm, corresponding to the average shear band thickness measured previously when no voids are present [9]. The shear offset lengths, the thickness of the considered shear band and the estimated strain in zones S1-up, S2-up and S3-up are given in Table 1, as well as the associated shear speed (as discussed below).

	Δz [µm]	2h [µm]	γ [/]	v_s [m s^{-1}]
Zone S1-up	4-7 ± 7	0.16-0.52 ± 0.03	14-20 ± 4	35 ± 8
Zone S2-up	12-15 ± 6	1 ± 0.2	12-15 ± 9	100 ± 6
Zone S3-up	30 ± 5	1 ± 0.2	30 ± 11	75 ± 10

Table 1 Estimation of the shear offset Δz, shear band thickness 2h, averaged shear strain γ and shear speed v_s for zones S1-up, S2-up and S3-up, respectively, given as average and standard deviation.

The strain level is more difficult to estimate in zone S4-up, as the shear offset at which damage nucleation occurs is unknown. However, the largest strain level is expected in zone S4-up because of the additional strong elongation of the micro-ligament (on which sample S4 was extracted) during the coalescence event.

4.2.2. Temperature evolution

During the fracture of Ti-12Mo, large variations of crack propagation speed and associated local temperature rise were measured by high speed imaging and the fusible coating method in our previous work [10], [11]. The tools developed in this previous work can be applied here to the extracted TEM samples to estimate the local temperature reached in these particular locations. The distribution of the maximum temperature reached can be estimated from the local production of heat in the localized shear band by considering a one-dimensional heat diffusion model:

$$\frac{\partial \Delta T}{\partial t} = \alpha \frac{\partial^2 \Delta T}{\partial x^2} + \frac{\dot{\omega}}{\rho C_p},$$

in which the heat release rate $\dot{\omega}$ is given by the local mechanical work rate, $\dot{\omega} = \beta . \tau . \frac{v_s}{2h}$ [J m^{-3} s^{-1}], during shear banding and with β being the Taylor-Quinney coefficient taken as 0.9; τ is the true shear

stress estimated as 700 MPa from the true axial fracture stress [10]; v_s is the shear speed and $2h$ the thickness of the shear band. Outside of the shear band and after shear banding, the heat release rate is taken as zero. The time of shear banding is estimated from the ratio between the local shear distance Δz from the edge of the fracture surface and the local shear speed v_s. To avoid an overestimation of the temperature in the shear band, the shear band is not considered as purely adiabatic and heat diffusion is considered. The maximum allowed temperature is bounded by the melting temperature of the alloy ($\mathrm{T_m} = 1700°\mathrm{C}$).

A similar evolution of the crack propagation speed with the length of the crack extension was observed for several cracks in Ti-12Mo owing to high-speed imaging [11]. During the formation of the shear surface from which sample S1 was extracted, a relatively low shear speed / heat rate is assumed as no Taylor meniscus patterns were observed on the fracture surface, while a larger shear speed / heat rate is expected for samples S2, S3 and S4 as melting patterns were observed at the positions where they were extracted on the fracture surface. The local shear speeds estimated for samples S1, S2 and S3 based on these measurements are given in Table 1 (more details can be found in [10], [11]). The field of maximum temperature reached in samples S1, S2 and S3 was computed based on the averaged value of these parameters, and is presented in Figure 12. A standard deviation of 365°C, 272°C and 419°C was estimated for the maximum temperature reached in samples S1, S2 and S3, respectively. These parameters could not be computed for sample S4, as explained hereafter. Table 2 summarizes the ratio of the maximum temperature reached in these samples with respect to the melting temperature of Ti-12Mo for the different zones identified in the TEM samples, as well as the estimated time during which dynamic recrystallization can be activated, i.e. when the temperature is higher than 40% of the melting temperature (520°C in the case of Ti-12Mo).

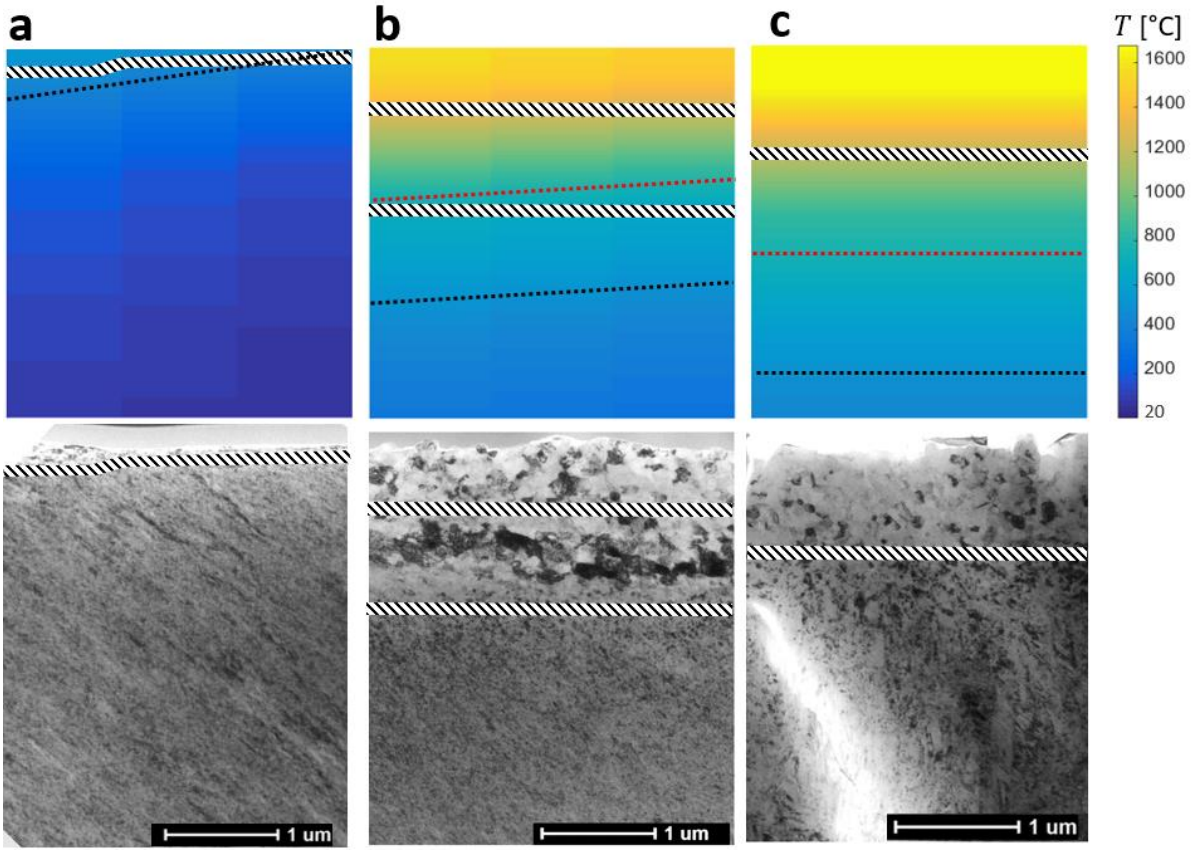

Figure 12: Estimation of the maximum temperature reached in samples (a) S1, (b) S2 and (c) S3, together with the reproduction of the associated bright field TEM micrographs for the sake of comparison. The dashed lines correspond to the transition between the different microstructures formed in the different zones in each sample. The red and black dotted lines correspond to the isotherm lines at 800°C ($T_{\beta-transus}$) and 520°C ($0.4T_m$), respectively.

TEM sample	**Zone**	T_{max}/T_m **[/]**	**t for T>0.** $4T_m$ **[µs]**
S1	S1-up	0.4-0.5	0.1-1
	S1-down	<0.4	<0.1
S2	S2-up	0.6-0.8	0.3-0.5
	S2-middle	0.4-0.7	<0.4
	S2-down	<0.4	<0.2
S3	S3-up	0.6-1	1.5-1.7
	S3-down	<0.6	<1.5

Table 2: Estimation of the maximum temperature normalized by the melting temperature of Ti-12Mo (T_{max}/T_m) and time spent above 40% of the melting temperature (t for $T>0.4T_m$) in each zone of the TEM samples based on the parameters given in Table 1.

The distribution of the temperature rise in sample S4 is more difficult to estimate as shear banding was followed by an intense tensile deformation in the micro-ligaments during the growth and coalescence of the voids. However, circular equiaxed dimples such as the one on which sample S4 was extracted (Figure 2(a)) are generally formed when the melting temperature of the alloy is reached in

the shear band (contrarily to elongated shear dimples formed when the local temperature during the formation of the cavities is lower [48]). These micro-ligaments are rapidly stretched causing further increase of the local temperature after the nucleation of these equiaxed dimples [49]. The temperature and time over 40% of the melting temperature are therefore considered to be the largest in zone S4-up amongst the different samples.

4.2.3. Microstructural evolution during fracture

The four TEM samples represent the modification of the microstructure during the propagation of the crack, corresponding to increasing strain levels and temperature rises from sample S1 to sample S4, as discussed in the previous sections. Figure 13 presents the proposed scenario of evolution of the microstructure during the shear banding and fracture of Ti-12Mo based on these observations.

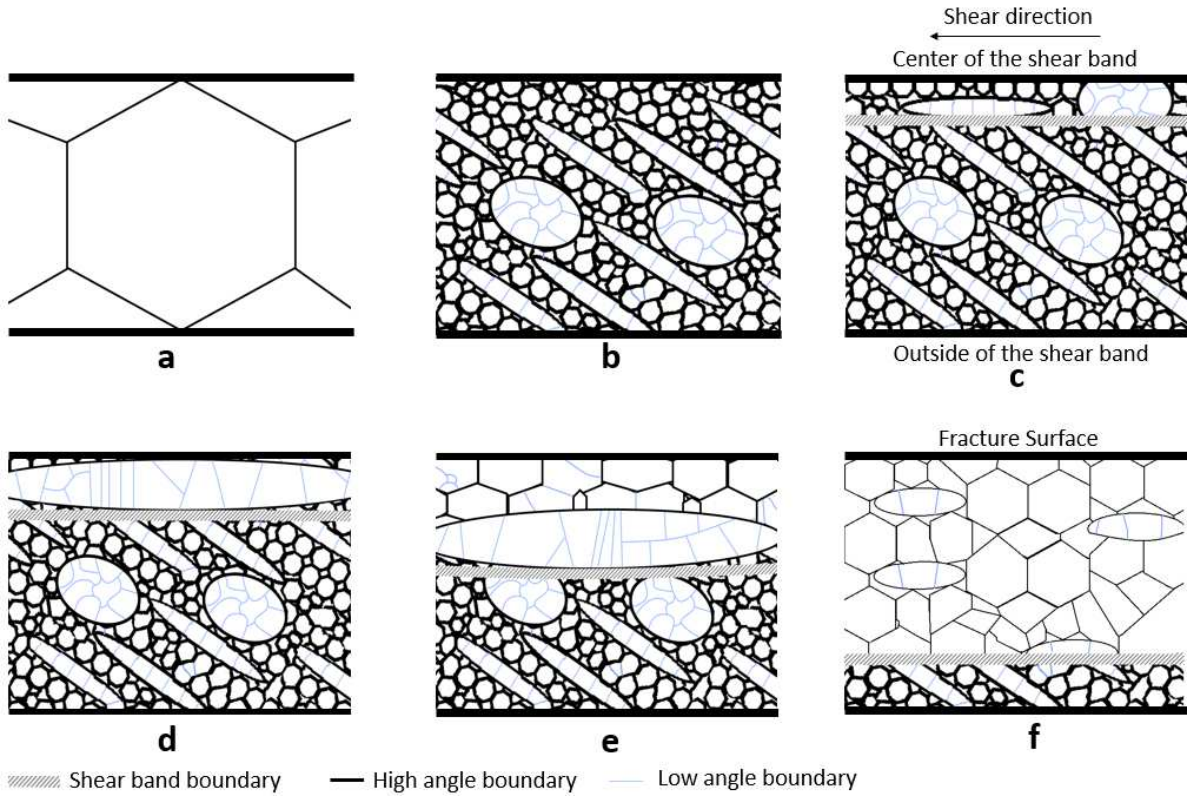

Figure 13: Schematic representation of the microstructure evolution of Ti-12Mo during its deformation to fracture. (a) Initial microstructure, (b) strongly deformed microstructure at the end of localized necking, (c) initiation of adiabatic shear banding, (d) dynamic recovery, (e) beginning of dynamic recrystallization, (f) end of the deformation.

The initial microstructure of Ti-12Mo is constituted of large equiaxed β grains (Fig. 13(a)). During its quasi-static deformation, many interfaces are created due to the activation of both TRIP and TWIP effects and the associated large work-hardening, inducing a SPD microstructure with nanograins containing nanocells (Fig. 13(b)). Fracture process begins by the localization of the deformation in a very thin shear band [11]. The shear speed, hence the local temperature, is relatively low, so that no significant thermally-activated microstructural transformation occurs. The elongated grains are simply rotated parallel to the shear direction in the shear band (Fig. 13(c)).

As the crack propagates, the shear speed increases, inducing a local temperature rise. Dynamic recovery is activated, and the dislocations are reorganized into long elongated grains to decrease the energy of the system (Fig. 13(d), corresponding to zone S2-middle in Figure 7). As the shear offset and/or the shear speed increases, the temperature and strain level increase also. Dynamic recrystallization is activated in the center of the shear band while dynamic recovery seems favored further away from the center of the shear band (Fig. 13(e)), as observed in Figure 7). An increase of the temperature above the β-transus temperature, followed by a large cooling rate (estimated in the order of magnitude of $10^9\ \mathrm{K\,s^{-1}}$ because of the short shearing time of about 0.3 µs), offers the thermodynamic and kinetic conditions for the precipitation of the ω_{ath} phase. The presence of ω_{ath} nanoprecipitates in the zones L2-up, L3-up and L4-up proves that a significant temperature rise was indeed reached in these regions, while no significant temperature increase occurred in zone L1-up.

Eventually, dynamic recrystallization is activated over a larger width, up to 1.6 µm from the fracture surface, with the additional strain level and temperature rise brought by the last step of fracture, i.e. the coalescence of the cavities in the center of the tensile specimen (Fig. 13(f), observed in Figures 8 and 9). The larger temperature increase obtained in the last step of the fracture process could explain the presence of ω_{ath} nanoprecipitates further away from the fracture surface, in zone L4-down. The dynamic recrystallization process is however incomplete as several cells and partly LAGB/partly HAGB boundaries are still found in the recrystallized zone, in zone L4-up.

Despite this careful analysis, some questions remain unanswered. Particularly, it would worth considering how these microstructural changes interact with the damage mechanisms in order to assess if dynamic recovery and dynamic recrystallization are beneficial or detrimental to the ductility of β −metastable TRIP-TWIP Ti alloys. The presented results nevertheless bring some preliminary answers. Indeed, dynamic recrystallization cannot be detrimental to the ductility of the alloy as dynamic recrystallization is only activated during the crack propagation, after fracture initiation. Void nucleation probably occurred by thermal softening in the center of the shear band, and is therefore concurrent to the occurrence of dynamic recovery and recrystallization. In that sense, it would be interesting to carry out the same microstructural analysis to the fracture surface of cylindrical tensile specimens of Ti-12Mo, in which shear banding is hindered, hence in which the fracture initiation differs from the one occurring here.

Conclusion

The microstructural evolution of β −metastable TRIP-TWIP Ti-12 Mo during its fracture occurring in thin adiabatic shear bands was studied. TEM samples were extracted from different zones corresponding to various fracture patterns on the fracture surface, to follow the microstructural evolution during the fracture process. The local strain levels and temperature distribution in the different TEM samples were estimated and used to interpret the observed microstructures. A local temperature close to the melting temperature on the fracture surface was reported in our previous work after quasi-static tensile loading at room temperature of this alloy. We show here that this very large increase of the temperature also induces thermally-activated modifications of the microstructure.

A severely deformed microstructure is initially formed by quasi-static tensile deformation, with equiaxed and elongated nano-cell blocks. In the beginning of adiabatic shear banding, the level of shear strain and temperature is relatively low, and the nanostructure is simply rotated parallel to the shear direction, together with low levels of dynamic recovery. With the local increase of shear strain and temperature, dynamic recrystallization is identified close to the fracture surface while dynamic

recovery seems favored further away from the fracture zone. Nanoprecipitates of ω_{ath} initially present in the microstructure before loading were dissolved during the quasi-static tensile loading and re-precipitated in the dynamic recrystallized region.

Acknowledgments

The Fonds National de la Recherche Scientifique FNRS is gratefully acknowledged for the grant n°T.0127.19 and the research grant of LC. H.I. is mandated by the Belgian National Fund for Scientific Research (FSR-FNRS)".

References

[1] M. Marteleur, F. Sun, T. Gloriant, P. Vermaut, P. J. Jacques, and F. Prima, "On the design of new β-metastable titanium alloys with improved work hardening rate thanks to simultaneous TRIP and TWIP effects," *Scripta Materialia*, vol. 66, no. 10, pp. 749–752, 2012, doi: 10.1016/j.scriptamat.2012.01.049.

[2] F. Sun *et al.*, "Investigation of early stage deformation mechanisms in a metastable beta titanium alloy showing combined twinning-induced plasticity and transformation-induced plasticity effects," *Acta Materialia*, vol. 61, no. 17, pp. 6406–6417, 2013, doi: 10.1016/j.actamat.2013.07.019.

[3] M. Ahmed, D. Wexler, G. Casillas, M. Ivasishin, and E. V Pereloma, "The influence of beta phase stability on deformation mode and compressive mechanical properties of Ti – 10V – 3Fe – 3Al alloy," *Acta Materialia*, vol. 84, pp. 124–135, 2015, doi: 10.1016/j.actamat.2014.10.043.

[4] F. Sun *et al.*, "A new titanium alloy with a combination of high strength, high strain hardening and improved ductility," *Scripta Materialia*, vol. 94, pp. 17–20, 2015, doi: 10.1016/j.scriptamat.2014.09.005.

[5] C. Brozek *et al.*, "A β-titanium alloy with extra high strain-hardening rate: Design and mechanical properties," *Scripta Materialia*, vol. 114, pp. 60–64, 2016, doi: 10.1016/j.scriptamat.2015.11.020.

[6] J. L. Zhang, C. C. Tasan, M. J. Lai, D. Yan, and D. Raabe, "Partial recrystallization of gum metal to achieve enhanced strength and ductility," *Acta Materialia*, vol. 135, pp. 400–410, 2017, doi: 10.1016/j.actamat.2017.06.051.

[7] L. Lilensten *et al.*, "On the heterogeneous nature of deformation in a strain-transformable beta metastable Ti-V-Cr-Al alloy," *Acta Materialia*, vol. 162, pp. 268–276, 2018, doi: 10.1016/j.actamat.2018.10.003.

[8] J. Gao *et al.*, "Segregation mediated heterogeneous structure in a metastable β titanium alloy with a superior combination of strength and ductility," *Scientific Reports*, vol. 8, no. 1, pp. 1–11, 2018, doi: 10.1038/s41598-018-25899-3.

[9] L. Choisez, L. Ding, M. Marteleur, H. Idrissi, T. Pardoen, and P. J. Jacques, “High temperature rise dominated cracking mechanisms in ultra-ductile and tough titanium alloy,” *Nature Communications*, vol. 11, no. 1, pp. 1–8, 2020, doi: 10.1038/s41467-020-15772-1.

[10] L. Choisez, G. Roy, and P. J. Jacques, “Temperature rise up to melting under quasi-static loading conditions induced by adiabatic shear banding,” *Materials and Design*, vol. 212, Dec. 2021, doi: 10.1016/j.matdes.2021.110269.

[11] L. Choisez, A. Elmahdy, P. Verleysen, and P. J. Jacques, “Fracture mechanisms in flat and cylindrical tensile specimens of TRIP-TWIP β-metastable Ti-12Mo alloy,” *Acta Materialia*, vol. 220, Nov. 2021, doi: 10.1016/j.actamat.2021.117294.

[12] G. Taylor, “The instability of liquid surfaces when accelerated in a direction perpendicular to their planes.,” in *Proceedings of the Royal Society of London A: Mathematical, Physical and Engineering Sciences*, 1950, vol. 201, no. 1065, pp. 192–19.

[13] A. S. Argon and M. Salama, “The mechanism of fracture in glassy materials capable of some inelastic deformation,” *Materials Science and Engineering*, vol. 23, no. 2–3, pp. 219–230, 1976, doi: 10.1016/0025-5416(76)90198-1.

[14] K. Huang and R. E. Logé, “A review of dynamic recrystallization phenomena in metallic materials,” *JMADE*, vol. 111, pp. 548–574, 2016, doi: 10.1016/j.matdes.2016.09.012.

[15] R. D. Doherty *et al.*, “Current issues in recrystallization: A review,” *Materials Science and Engineering A*, vol. 238, no. 2, pp. 219–274, 1997, doi: 10.1016/S0921-5093(97)00424-3.

[16] L. Guo, X. Fan, G. Yu, and H. Yang, “Microstructure control techniques in primary hot working of titanium alloy bars: A review,” *Chinese Journal of Aeronautics*, vol. 29, no. 1, pp. 30–40, 2016, doi: 10.1016/j.cja.2015.07.011.

[17] B. Derby, “The dependence of grain size on stress during dynamic recrystallisation,” *Acta Metallurgica Et Materialia*, vol. 39, no. 5, pp. 955–962, 1991, doi: 10.1016/0956-7151(91)90295-C.

[18] T. Sakai, A. Belyakov, R. Kaibyshev, H. Miura, and J. J. Jonas, “Dynamic and post-dynamic recrystallization under hot, cold and severe plastic deformation conditions,” *Progress in Materials Science*, vol. 60, no. 1, pp. 130–207, 2014, doi: 10.1016/j.pmatsci.2013.09.002.

[19] F. Montheillet, L. Pallot, and D. Piot, “Hot deformation and dynamic recrystallization of the beta phase in titanium alloys,” *Materials Science Forum*, vol. 706–709, pp. 127–134, 2012, doi: 10.4028/www.scientific.net/MSF.706-709.127.

[20] Y. Chen, J. Li, B. Tang, H. Kou, X. Xue, and Y. Cui, “Texture evolution and dynamic recrystallization in a beta titanium alloy during hot-rolling process,” *Journal of Alloys and Compounds*, vol. 618, pp. 146–152, 2015, doi: 10.1016/j.jallcom.2014.08.129.

[21] H. J. McQueen, “Development of dynamic recrystallization theory,” *Materials Science and Engineering A*, vol. 387–389, no. 1-2 SPEC. ISS., pp. 203–208, 2004, doi: 10.1016/j.msea.2004.01.064.

[22] H. Li, C. Wu, and H. Yang, “Crystal plasticity modeling of the dynamic recrystallization of two-phase titanium alloys during isothermal processing,” *International Journal of Plasticity*, vol. 51, pp. 271–291, 2013, doi: 10.1016/j.ijplas.2013.05.001.

[23] Y. Yang and B. F. Wang, “Dynamic recrystallization in adiabatic shear band in α-titanium,” *Materials Letters*, vol. 60, no. 17–18, pp. 2198–2202, 2006, doi: 10.1016/j.matlet.2005.12.097.

[24] Y. Yang, F. Jiang, B. M. Zhou, X. M. Li, H. G. Zheng, and Q. M. Zhang, “Microstructural characterization and evolution mechanism of adiabatic shear band in a near beta-Ti alloy,” *Materials Science and Engineering A*, vol. 528, no. 6, pp. 2787–2794, 2011, doi: 10.1016/j.msea.2010.12.053.

[25] Z. X. Du, J. S. Liu, S. D. Jiang, S. L. Xiao, F. T. Kong, and Y. Y. Chen, “Strain rate dependence of microstructural evolution in β titanium alloy during subtransus superplastic deformation,” *Journal of Alloys and Compounds*, vol. 647, pp. 1–5, 2015, doi: 10.1016/j.jallcom.2015.06.070.

[26] J. Zhao, J. Zhong, F. Yan, F. Chai, and M. Dargusch, “Deformation behaviour and mechanisms during hot compression at supertransus temperatures in Ti-10V-2Fe-3Al,” *Journal of Alloys and Compounds*, vol. 710, pp. 616–627, 2017, doi: 10.1016/j.jallcom.2017.03.219.

[27] X. G. Fan, H. Yang, P. F. Gao, R. Zuo, and P. H. Lei, “The role of dynamic and post dynamic recrystallization on microstructure refinement in primary working of a coarse grained two-phase titanium alloy,” *Journal of Materials Processing Technology*, vol. 234, pp. 290–299, 2016, doi: 10.1016/j.jmatprotec.2016.03.031.

[28] R. Dong, J. Li, H. Kou, B. Tang, K. Hua, and S. Liu, “Characteristics of a hot-rolled near β titanium alloy Ti-7333,” *Materials Characterization*, vol. 129, no. January, pp. 135–142, 2017, doi: 10.1016/j.matchar.2017.04.031.

[29] H.-Q. Chen, C.-X. Cao, L. Guo, and H. Lin, “Hot deformation mechanism and microstructure evolution of TC11 titanium alloy in β field,” *Transactions of Nonferrous Metals Society of China (English Edition)*, vol. 18, no. 5, pp. 1021–1027, 2008, doi: 10.1016/S1003-6326(08)60175-2.

[30] J. Fan, J. Li, H. Kou, K. Hua, B. Tang, and Y. Zhang, “Microstructure and mechanical property correlation and property optimization of a near beta titanium alloy Ti-7333,” *Journal of Alloys and Compounds*, vol. 682, pp. 517–524, 2016, doi: 10.1016/j.jallcom.2016.04.303.

[31] M. Marteleur, H. Idrissi, B. Amin-Ahmadi, F. Prima, D. Schryvers, and P. J. Jacques, “On the nucleation mechanism of {112} 〈111〉 mechanical twins in as-quenched β metastable Ti-12 wt.% Mo alloy,” *Materialia (Oxf)*, vol. 7, no. April 2019, 2019, doi: 10.1016/j.mtla.2019.100418.

[32] A. Gysler, G. Lütjering, and V. Gerold, “Deformation behavior of age-hardened Ti-Mo alloys,” *Acta Metallurgica*, vol. 22, no. 7, pp. 901–909, 1974, doi: 10.1016/0001-6160(74)90057-1.

[33] W. Chen *et al.*, “Strong deformation anisotropies of \omega-precipitates and strengthening mechanisms in Ti-10V-2Fe-3Al alloy micropillars: Precipitates shearing vs precipitates disordering,” *Acta Materialia*, vol. 117, pp. 68–80, 2016, doi: 10.1016/j.actamat.2016.06.065.

[34] L. A. I. Kestens and H. Pirgazi, “Texture formation in metal alloys with cubic crystal structures,” *Materials Science and Technology*, vol. 32, no. 13, pp. 1303–1315, 2016, doi: 10.1080/02670836.2016.1231746.

[35] B. Sander and D. Raabe, “Texture inhomogeneity in a Ti-Nb-based β-titanium alloy after warm rolling and recrystallization,” *Materials Science and Engineering A*, vol. 479, no. 1–2, pp. 236–247, 2008, doi: 10.1016/j.msea.2007.06.077.

[36] M. A. Meyers, J. C. LaSalvia, V. F. Nesterenko, Y. J. Chen, and B. K. Kad, “Dynamic Recrystallization in High Strain Rate Deformation,” *The Third International Conference on Recrystallization and Related Phenomena*. pp. 279–286, 1997.

[37] V. F. Nesterenko, M. a. Meyers, J. C. LaSalvia, M. P. Bondar, Y. J. Chen, and Y. L. Lukyanov, “Shear localization and recrystallization in high-strain, high-strain-rate deformation of tantalum,” *Materials Science and Engineering: A*, vol. 229, no. 1–2, pp. 23–41, 1997, doi: 10.1016/S0921-5093(96)10847-9.

[38] N. Bozzolo, N. Dewobroto, T. Grosdidier, and F. Wagner, “Texture evolution during grain growth in recrystallized commercially pure titanium,” *Materials Science and Engineering A*, vol. 397, no. 1–2, pp. 346–355, 2005, doi: 10.1016/j.msea.2005.02.049.

[39] H. Jiang, P. Dong, S. Zeng, and B. Wu, “Effects of Recrystallization on Microstructure and Texture Evolution of Cold-Rolled Ti-6Al-4V Alloy,” *Journal of Materials Engineering and Performance*, vol. 25, no. 5, pp. 1931–1938, 2016, doi: 10.1007/s11665-016-2006-7.

[40] Z. Li, B. Wang, S. Zhao, R. Z. Valiev, K. S. Vecchio, and M. A. Meyers, “Dynamic deformation and failure of ultrafine-grained titanium,” *Acta Materialia*, vol. 125, pp. 210–218, 2017, doi: 10.1016/j.actamat.2016.11.041.

[41] M. A. Meyers and H. R. Pak, “Observation of an adiabatic shear band in titanium by high-voltage transmission electron microscopy,” *Acta Metallurgica*, vol. 34, no. 12, pp. 2493–2499, 1986, doi: 10.1016/0001-6160(86)90152-5.

[42] M. A. Meyers, V. F. Nesterenko, J. C. LaSalvia, and Q. Xue, “Shear localization in dynamic deformation of materials: Microstructural evolution and self-organization,” *Materials Science and Engineering A*, vol. 317, no. 1–2, pp. 204–225, 2001, doi: 10.1016/S0921-5093(01)01160-1.

[43] V. Tvergaard, “Necking in tensile bars with rectangular cross-section,” *Computer Methods in Applied Mechanics and Engineering*, vol. 103, no. 1–2, pp. 273–290, 1993, doi: 10.1016/0045-7825(93)90049-4.

[44] A. A. Popov *et al.*, “Structural and mechanical properties of nanocrystalline titanium processed by severe plastic deformation,” *Scripta Materialia*, vol. 37, no. 7, pp. 1089–1094, 1997, doi: 10.1016/S1359-6462(97)00210-8.

[45] R. S. Mishra, V. V. Stolyarov, C. Echer, R. Z. Valiev, and A. K. Mukherjee, “Mechanical behavior and superplasticity of a severe plastic deformation processed nanocrystalline Ti–6Al–4V alloy,” *Materials Science and Engineering: A*, vol. 298, no. 1–2, pp. 44–50, 2001, doi: 10.1016/s0921-5093(00)01338-1.

[46] A. Zafari, X. S. Wei, W. Xu, and K. Xia, “Formation of nanocrystalline β structure in metastable beta Ti alloy during high pressure torsion: The role played by stress induced martensitic transformation,” *Acta Materialia*, vol. 97, pp. 146–155, 2015, doi: 10.1016/j.actamat.2015.06.042.

[47] J. Y. Zhang, J. S. Li, Z. Chen, Q. K. Meng, F. Sun, and B. L. Shen, “Microstructural evolution of a ductile metastable β titanium alloy with combined TRIP/TWIP effects,” *Journal of Alloys and Compounds*, vol. 699, pp. 775–782, 2017, doi: 10.1016/j.jallcom.2016.12.394.

[48] A. Shahan and A. Karimi Taheri, “Adiabatic shear bands in titanium and titanium alloys: a critical review,” *Materials & Design*, vol. 14, no. 4, pp. 243–250, 1993, doi: 10.1016/0261-3069(93)90078-A.

[49] J. D. Bryant, D. D. Makel, and H. G. F. Wilsdorf, “Observations on the effect of temperature rise at fracture in two titanium alloys,” *Materials Science and Engineering*, vol. 77, no. C, pp. 85–93, 1986, doi: 10.1016/0025-5416(86)90356-3.